Cryogenics 141 (2024) 103888

Contents lists available at ScienceDirect

Cryogenics

journal homepage: www.elsevier.com/locate/cryogenics

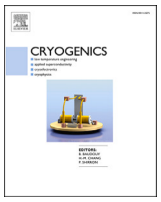

An experimental and numerical framework to assess the temperature distribution in complex He II-cooled magnet geometries

Kirtana Puthran [a,*], Patricia Borges de Sousa [a], Lise Murberg [a,b], Torsten Koettig [a], Rob van Weelderen [a]

[a] CERN, Esplanade des Particules 1, 1211 Geneva 23, Switzerland
[b] Norwegian University of Science and Technology (NTNU), Trondheim, Norway

A B S T R A C T

In the context of the High Luminosity upgrade of the Large Hadron Collider at CERN, a framework implementing experimental techniques and numerical analysis has been developed to systematically assess the temperature distribution in complex He II-cooled composite magnet geometries. The experiments are designed to measure the heat transfer coefficients in the magnet coil layers using coil samples in a stagnant superfluid helium bath. A numerical tool-kit has been developed to facilitate intensive parametric studies, in addition to estimation of helium content via a phenomenological model. The workflow of the tool-kit is built to handle complex geometries composed of different materials each with their temperature-dependent properties, at low computational cost. This framework has been validated with experimental data obtained from laboratory-scale experiments on impregnated coil samples, reported and discussed here. Three use cases for the developed numerical tool, with increasing levels of complexity, are presented and its results discussed.

1. Introduction

The cooling requirements of superconducting accelerator magnets entail, in addition to their working temperature, the reduction of thermal stresses which they are subjected to in the form of radiation-induced heat deposition due to particle losses from beams and beam collision debris. Contrary to the NbTi accelerator magnets currently operational in the Large Hadron Collider (LHC) [1], the impregnated Nb_3Sn magnets for the High-Luminosity upgrade (HL-LHC) [2] are not in direct contact with the cooling fluid, superfluid helium [3]. The internal or external heat loads in the superconducting cable layers are removed by pure conduction to the cold source, through a stagnant, subcooled He II bath. The heat loads are also not homogeneous in the radial and azimuthal directions, leading to a non-uniform temperature distribution across the cold mass structure. While a pressurised He II bath is a very efficient cooling medium [4], accurate evaluation of the local conductor temperatures in the coils is essential to ascertain that they are maintained below the critical surface for superconductivity, under expected thermal load conditions.

At the Central Cryogenics Laboratory at CERN, a framework to evaluate the heat transfer characteristics of the impregnated Nb_3Sn magnets has been proposed. The program encompasses experimental techniques to directly measure the heat transfer behaviour in magnet coil samples in representative conditions, accompanied by the development of a numerical tool-kit to simulate this behaviour and extrapolate it to full cross-sectional geometries of a magnet's cold mass, as designed for the accelerator upgrade. The main objective of this framework is to systematically assess the temperature fields and resulting theoretical margins in the magnet coils, and validate the heat extraction design of the cold mass under peak power deposition conditions at nominal luminosity.

This article reports observations and analysis from experimental measurements and details of the numerical tool-kit along with use cases to demonstrate the robust nature of the framework.

2. Experimental studies

For this program, a test station has been systematically developed to study the heat transfer characteristics of superconducting cables and coil samples in a superfluid helium bath. This station was initially used to characterise NbTi cable stacks [5,6]. It has subsequently been upgraded and is currently operational as part of the test program. A detailed description of the test station is reported elsewhere [7,8]. In this section, the experimental methods employed and observations obtained for two types of magnet [9–11] coil samples viz. D11T-GE02 and MQXF-P06, detailed in Table 1, each in their series production stages, are briefly described.

* Corresponding author.
E-mail addresses: kirtana.puthran@cern.ch (K. Puthran), pat.borges.sousa@cern.ch (P. Borges de Sousa), lise@murberg.no (L. Murberg), torsten.koettig@cern.ch (T. Koettig), rob.van.weelderen@cern.ch (R. van Weelderen).

https://doi.org/10.1016/j.cryogenics.2024.103888
Received 7 July 2023; Received in revised form 20 March 2024; Accepted 21 June 2024
Available online 1 July 2024

Table 1
Sample specifications.

	D11T-GE02	MQXF-P06
Cable parameters		
Number of strands	40	40
Nominal strand diameter [mm]	0.700	0.850
Average cable width [mm]	14.7	18.36
Average cable thickness [mm]	1.25	1.525
Cable insulation thickness [mm]	0.100	0.145
Cut sample parameters		
Inner radius [mm]	30	75
Cables in inner layer	9	7
Cables in outer layer	11	8
Inner insulation thickness* [mm]	0.45 - 0.5	0.7 - 0.9
Inter layer insulation thickness* [mm]	0.75 - 0.9	1.3 - 1.4
Exposed length [mm]	120	115

*Measured values.

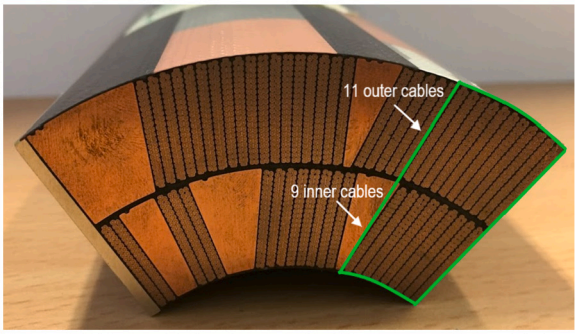

(a) Segment of the D11T-GE02 coil, with annular section of sample (to be cut) marked in green.

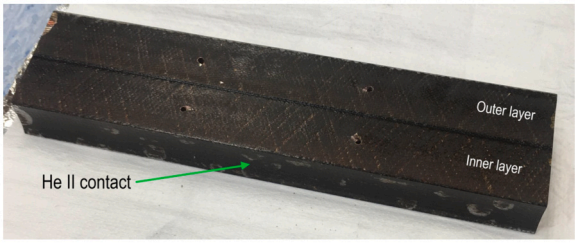

(b) Cut D11T-GE02 sample before insulation, with holes for temperature sensors in outer (TL, TR) and inner (BL, BR) cable layers and indication of the inner surface, which is exposed to the He II bath.

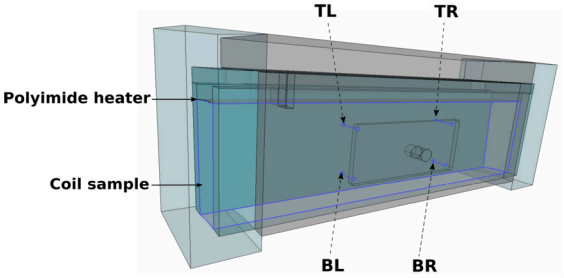

(c) Schematic of an insulated sample, shown with locations of temperature sensors and the polyimide heater placed on the outer surface of the coil sample.

Fig. 1. Sample preparation for experimental measurements. (For interpretation of the colours in the figure(s), the reader is referred to the web version of this article.)

2.1. Methods

The aim of the experiments is to measure the heat transfer characteristics of partially insulated magnet coil samples, which are submerged

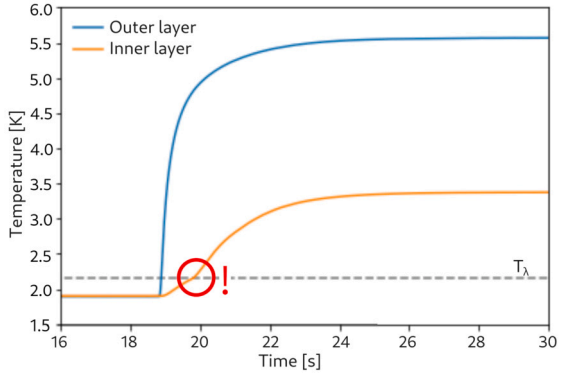

(a) Typical measurement data point, as recorded in this case for the D11T-GE02 sample. Kinks seen in inner layer temperature plots at T_λ are indicative of helium presence.

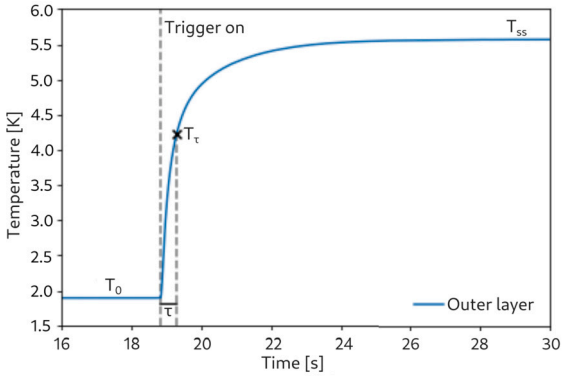

(b) Initial temperature, T_0, steady state temperature, T_{ss}, time constant τ and temperature T_τ are extracted for each layer, shown here for the outer layer, at each input heat load.

Fig. 2. Example of experiment data acquisition for one case of an applied heat load.

in a bath of pressurised He II. An example of an as-obtained D11T-GE02 coil segment is shown in Fig. 1a. A section of this segment (longer in length than the twist pitch of the cables) is cut out as marked in the figure. The cut sample is shown in Fig. 1b. Also seen in this figure, are holes of 1.4 mm diameter drilled into each cable layer at equal lengths from the ends, to place temperature sensors (LakeShore Cernox™ bare-chip thermometers) in the center of the cable layer cross-section in the azimuthal direction. This can be seen in the schematic shown in Fig. 1c. The sensors are insulated with low viscosity Stycast® and carefully placed inside the sample holes, which are then filled with high viscosity Stycast®. Great care is taken to avoid any voids in the process. An external polyimide heater foil is bonded to the outer radial surface of the sample, which is then insulated with a combination of low conductivity insulating material blocks of G-10 and Ultem® using high viscosity Stycast®. Importantly, the inner radial surface of the samples, marked in Fig. 1b, remains uninsulated and therefore directly exposed to the helium bath during the measurements, listed as *exposed length* for both the samples measured, in Table 1.

A typical measurement data point is shown in Fig. 2. The two sensor temperatures at each cable layer are averaged for analysis. On triggering the heater, as heat flows towards the helium bath, a rise in the temperatures of each layer is seen, with the outer layer reaching a higher steady-state temperature than the inner layer.

Assuming a lumped model for a thermal system cooled by an external bath at initial temperature T_0, the temperature T of the system at time t can be described by,

$$\frac{dT}{dt} = -\frac{1}{\tau}(T(t) - T_0) = -\frac{1}{\tau}(\Delta T(t)) \tag{1}$$

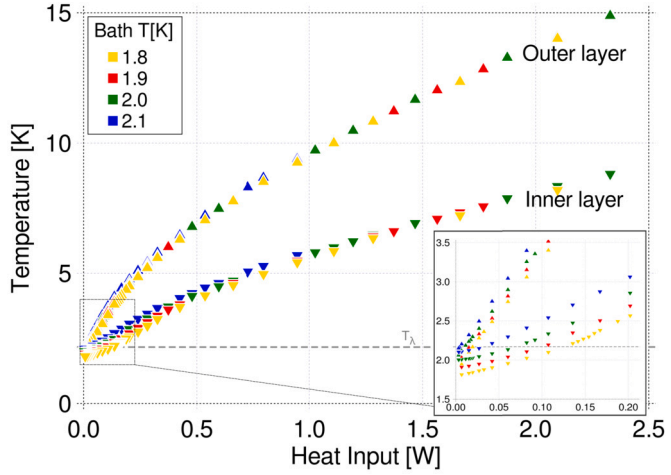

(a) Variation of steady state temperature, T_{ss} with heat input.

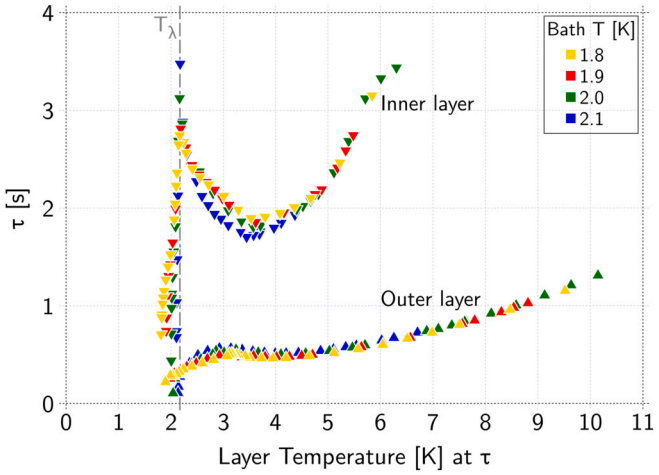

(b) Variation of time constants, τ with layer temperature T_τ.

Fig. 3. Measurement results for D11T-GE02 sample.

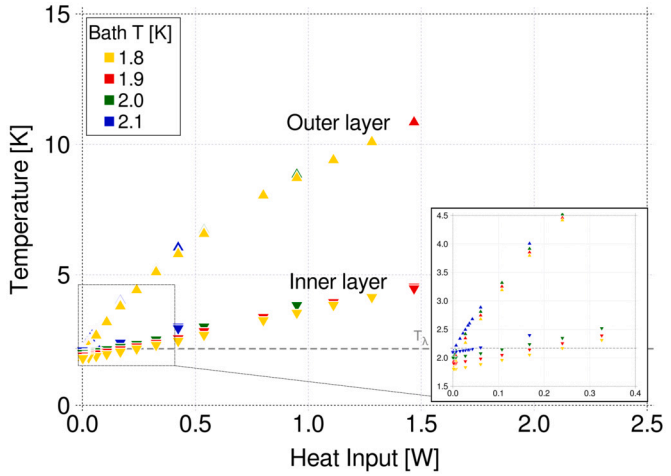

(a) Variation of steady-state temperature, T_{ss} with heat input.

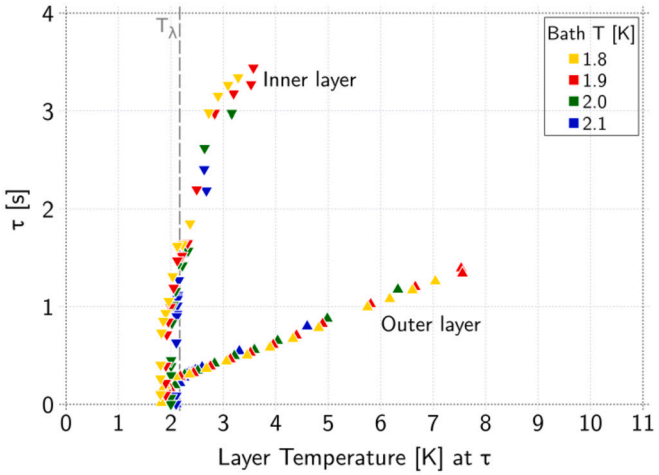

(b) Variation of time constants, τ with layer temperature T_τ.

Fig. 4. Measurement results for MQXF-P06 sample.

where τ is the characteristic time response of the system, *i.e.* the time for the system to reach $1 - 1/e \approx 63.2\%$ of the steady-state value. The solution to the equation (1) is given by,

$$T(t) = T_0 \cdot e^{-t/\tau}. \tag{2}$$

For each acquired measurement, the steady-state temperature of the cable layers T_{ss}, the time constant τ and the layer temperature T_τ at τ are extracted. The measurements are conducted for varying heat loads and bath temperatures ranging from 1.8 K to 2.1 K.

The measurement error on the helium bath temperature is ±2 mK up to 2.1 K and ±11 mK at 4.2 K. The cable layer temperature sensors, which are calibrated against the temperature sensor in the bath, have a maximum measurement error of ±3 mK at 2.1 K and ±50 mK at 4.2 K.

2.2. Measurement results & observations

The steady-state temperatures as a function of the input heat load and time constants as a function of the layer temperatures measured for the two coil samples, *i.e.* D11T-GE02 and MQXF-P06, are plotted in Fig. 3 and Fig. 4 respectively.

The main observations may be summarised as follows:

1. At low heat loads up to 0.5 W, an effect of the bath temperature on the steady state temperatures T_{ss} is pronounced for both samples. At high heat loads, T_{ss} obtained is irrespective of bath temperature for both samples.
2. For the D11T-GE02 sample, a peak in time constants measured for the inner cable layer is observed at T_λ of up to 3.44 s. A small peak is seen for the outer cable layer close to 3 K. A distinct effect of bath temperature is also seen in the inner cable layer time constants.
3. For the MQXF-P06 sample, a steady rise in time constants is measured. There are no peaks observed for either cable layer. An effect of bath temperature is also seen for the inner layer time constants.

The convergence of the steady-state temperatures at temperatures greater than 3 K irrespective of bath temperature, suggests that above this temperature, the thermal behaviour is dependent only on the material properties of the solid components of the system.

The peak seen in the transient behaviour of the samples was also previously measured in prototype samples [7]. This is attributed to the presence of some helium within the sample since He II has a peak in heat capacity at its transition temperature, T_λ.

Compared to the prototype samples wherein helium content was noted for both cable layers for both magnet sample types [7], the D11T-GE02 sample showed significant helium presence in only the inner cable layer, whereas for the MQXF-P06 sample, helium presence may be noted for inner cable layer only from steady state temperature curves and not at all from the transient curves. Improved vacuum impregnation

techniques [12] in the evolution of the magnet construction may have resulted in lower helium penetration.

3. Numerical model

In this study, the assessment of the temperature distribution in the Nb_3Sn magnets during operational conditions with a given input power deposition map using numerical models has been approached via two ways:

1. Modelling only the thermal conduction within the magnets, with a Neumann convection boundary condition at surfaces exposed to the cooling fluid (see sections 4.1 and 4.2).
2. A conjugate heat transfer model, wherein both the solid and fluid systems are solved separately, and exchange boundary condition data at each successive iteration (see section 4.3).

The main factors affecting the complexity of a numerical heat transfer model of He II-cooled superconducting magnet via both approaches are:

1. The complex composite structure of the Nb_3Sn magnet coils is resolvable to the micron scale [11,13–15]. For example, each cable is comprised of 40 wires, a stainless steel core and some epoxy resin after impregnation. The insulation system in itself is also a composite formulation of S2-glass fibre layers, CTD-101K® epoxy resin and CTD-1202® binder [12,16]. Reasonable approximations to the geometry must be made, such that the critical driving components of the thermal gradients, *i.e.* the insulating layers, are preserved.
2. The thermal properties of materials are temperature-dependent in cryogenic conditions. These are usually expressed as polynomial functions, which add heavily to run-time computation cost. In addition, available data in literature is either sparse or not available.
3. The phenomena of Kapitza or interface thermal boundary resistances at low temperatures result in discontinuous temperatures at the interface surfaces of helium and the solid material in contact.

Given these factors, the over-arching goals for the development of a numerical tool-kit are:

1. Development of a workflow to reduce initial uptake in generating high-quality conformal meshes, enabling refinement studies at the interfaces between the various components;
2. Development of numerical solvers capable of solving energy equations for static superfluid helium and solids with varying thermal properties;
3. Implementation of an interface resistance boundary condition;
4. Capability of easy parametrisation studies to predict and optimise operational requirements;

The development of the tool-kit has been undertaken using open-source software. The creation of the geometries and the numerical mesh has been undertaken using scripting in Salome-platform V9.7 [17]. The main numerical analysis is then carried out in OpenFOAM v7.0 [18], which is an open-source Finite Volume Method (FVM) based Computational Fluid Dynamics (CFD) toolbox.

3.1. Governing equations

For solid regions, transient heat conduction is governed by the equation,

$$\rho c_p(T)\frac{\partial T}{\partial t} = \nabla \cdot (k(T)\nabla T) + \dot{q} \tag{3}$$

where ρ is the density, and c_p and k are the temperature-dependent specific heat capacity and thermal conductivity respectively.

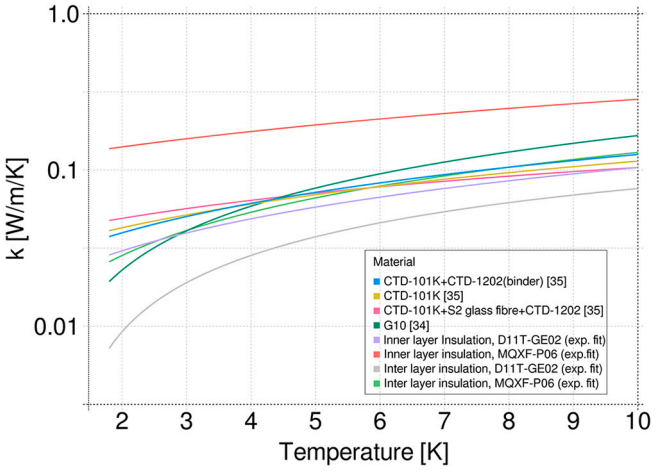

Fig. 5. Thermal conductivity as a function of temperature for S2 glass and epoxy resin insulation systems used for materials in the composite magnet models.

In case of a superfluid helium bath with no net mass flow condition, the two-fluid model is simplified [19,20] to the energy equation given by,

$$\rho c_p(T)\frac{\partial T}{\partial t} = \nabla \cdot (K_{eff}(T, \nabla T)T) + \dot{q} \tag{4}$$

where ρ is the density, c_p is the specific heat capacity and K_{eff} is the effective thermal conductivity of helium. The implementation of the effective thermal conductivity used here is elaborated in section 3.3.

3.2. Solid material properties

The assignment of appropriate material properties is critical to the accuracy of numerical calculations. As aforementioned, the thermal properties of materials are temperature-dependent at cryogenic temperatures. Due to the composite nature of the superconductor wires, cables, and their insulation schemes and the complex fabrication process involved, these properties also have to be extracted indirectly during measurements [21–23]. A non-exhaustive literature review of available measured properties [24–34] shows a dispersion in the measured data. A series of in-house measurements [35,36] to obtain the thermal conductivity of D11T magnet samples has also been carried out.

To reiterate, depending on the problem at hand, an appropriate approximation of the geometry must be made for numerical simulations. For the heat transfer case studies, a cable is homogenised as a single region assuming that the highly conductive copper matrix contribution and the Rutherford-type geometry ensures an even temperature across the width of the cables. The insulation layers, which are composites of glass fibre layers and epoxy resin of different thicknesses, are also homogenised as a single region.

The thermal conductivity of the insulation systems, comparing some data from literature [34,35] to those obtained from the experimental studies reported in this article (see section 4.1), is shown in Fig. 5. The heat capacity data used for the simulations is shown in Fig. 6. For the cable layers, they are derived as a function of the volumetric composition of the components.

3.3. He II properties

The density ρ and specific heat capacity c_p of superfluid helium are extracted from HePak [37], which is a series of physics-based fundamental state equations for calculating the thermophysical properties of helium-4.

For He II, in steady-state heat transport from the two-fluid model, if there is no net mass flow, the temperature gradient is given by,

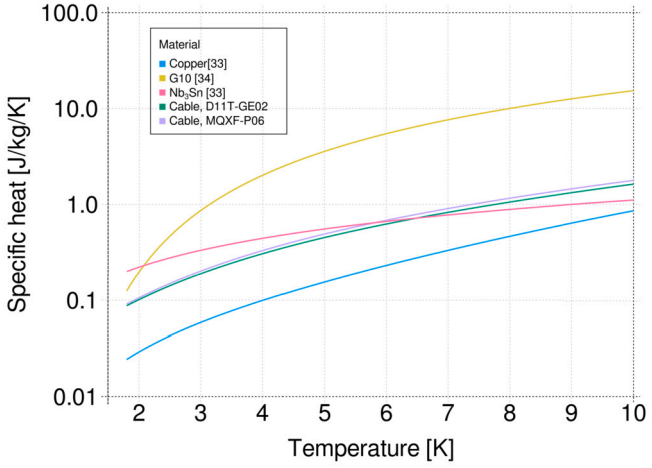

Fig. 6. Specific heat capacity as a function of temperature used for materials in the composite magnet models.

$$\nabla T = -\frac{\beta \mu_n q}{d^2 (\rho s)^2 T} - f(T,p) q^m \tag{5}$$

where the thermal conductivity in Landau or laminar flow regime [38], which occurs below a critical flow velocity, especially in the case of low velocities in narrow channels, is

$$K_L(T) = -\frac{d^2 (\rho s)^2 T}{\beta \mu_n} \tag{6}$$

where ρ, s, μ_n are density, entropy and dynamic viscosity, and d and β are the diameter and shape factor respectively. In the Gorter-Mellink or turbulent flow regime [39] the thermal conductivity is given by,

$$K_{GM}(T, \nabla T) = \left(\frac{f^{-1}(T,p)}{|\nabla T|^2} \right)^{\frac{1}{m}} \tag{7}$$

where $f^{-1}(T,p)$ is a thermal conductivity function. In this study, Sato's empirical correlations [40,41] are used, with $m = 3.4$.

For practical applications where helium is used as a technical coolant, such as for superconducting devices, conductive heat transport is considered to be in turbulent or Gorter-Mellink regime [42], where the effective thermal conductivity is as given by equation (7) and the normal fluid viscous term is neglected. However, for a homogeneous initial condition, $|\nabla T| = 0$ in the denominator is a singularity. This is avoided by using a direct transition model for effective thermal conductivity [5,6],

$$K_{Eff} = \begin{cases} K_L(T) & \text{if } |\nabla T| < \gamma(T) \\ K_{GM}(T, \nabla T) & \text{if } |\nabla T| \geq \gamma(T) \end{cases} \tag{8}$$

where $\gamma(T)$ is a temperature-dependent critical gradient given by,

$$\gamma(T) = f^{-\frac{1}{m-1}} \left(\frac{d^2}{\beta} \frac{(\rho s)^2 T}{\mu_n} \right)^{-\frac{m}{m-1}}. \tag{9}$$

It is worth noting that β and d used in the laminar regime are defined for small geometries and in reality, a transition regime exists.

3.4. Kapitza interface boundary condition

Of importance to the cooling studies of superconducting magnets is the existence of an interface thermal resistance between solid materials and superfluid helium, called Kapitza resistance [19]. This resistance results in discontinuous and higher temperature at the interacting solid surface compared to that of the He II in contact. In general, this resistance depends on the local temperature of the superfluid helium, in addition to the material properties of the solid. While many theories explaining Kapitza resistance exist, experimental measurements are usually reported in the form of,

$$h_K = \alpha T^n \tag{10}$$

where h_K is the heat transfer coefficient and T is the temperature of He II at the interface. The quantities α and n are empirically determined quantities, with n in between 2 and 4.

Equation (10) may be directly used to implement a heat-flux Neumann boundary condition in case of a solid heat conduction-only model. Such a case therefore assumes no change in the local temperature of He II at the interface, and may be applied when a large stagnant He II bath is used as a coolant, but would not be appropriate for He II in thin channel geometries. For the latter, a conjugate heat transfer model, which updates the heat transfer coefficient according to the local variation in the temperature of the superfluid at the interface, may be essential.

The values of $\alpha = 35.05$ and 80.57, and $n = 3.38$ and 3.23 are empirically determined for the D11T-GE02 and MQXF-P06 samples, respectively, from the experimental measurements described earlier for $\Delta T_{ss} < 80$ mK, based on the assumption that the role of Kapitza resistance dominates the temperature gradient at very low heat fluxes.

3.5. Estimation of helium content

Heat and mass transfer of He II through porous media is well documented and reported. Several experimental [43–45] and numerical [46,47] studies have been reviewed for possibilities to implement a model for helium content estimation. Generally, the physical characteristics of the porous media such as pore size or porosity, permeability, specific surface area, and concept of tortuosity are used to describe heat transfer with Darcy's law for classical fluids in porous media. These characteristics are however not known for the composite magnet samples, and would also require a more intensive geometrical modelling at pore level, whereas a qualitative estimation of the helium content is considered sufficient for this program.

A phenomenological model is thus adopted to estimate the helium content observed in the experimental studies. For any cell in a solid region of the mesh, the contribution to volumetric heat capacity may be estimated with

$$(\rho c_p)_{cell} = (1 - \phi_v)(\rho c_p)_{solid} + \phi_v (\rho c_p)_{HeII} \tag{11}$$

where ϕ_v is the helium content by volume in that cell. The contribution to thermal conductivity is ignored with this model.

3.6. Implementation

In OpenFOAM, a *solver* is an application used to solve a specific continuum mechanics problem or equation. Three user-defined solvers have been created for the numerical tool-kit, *i.e.* for solving the governing equations for transient heat conduction in a composite solid given by equation (3), in superfluid helium given by equation (4), and a conjugate heat transfer multi-region solver combining the two. These solvers work in cohesion with dynamically-linked custom *libraries*, which compute the temperature-dependent thermal properties at run-time.

Modelling of heat transfer in solid-fluid or solid-solid systems is handled natively in OpenFOAM v7.0 by defining each component as a separate region, with an interface boundary condition between the regions. This equates to solving the discretized equations in matrix form for each region, while updating the boundary conditions at the interfaces at each iteration. Due to the composite structure of the magnets, this incurs heavy computation costs. To put this in perspective, the total number of separated solid regions modelled for the experimental coil samples is 8, while that of a coil pack is 250 and for a full scale magnet cross-section is ~500. Such multi-region models also result in very low to no scaling in terms of parallel computation. It is prohibitive to conduct a comprehensive parametric study with such high computation costs.

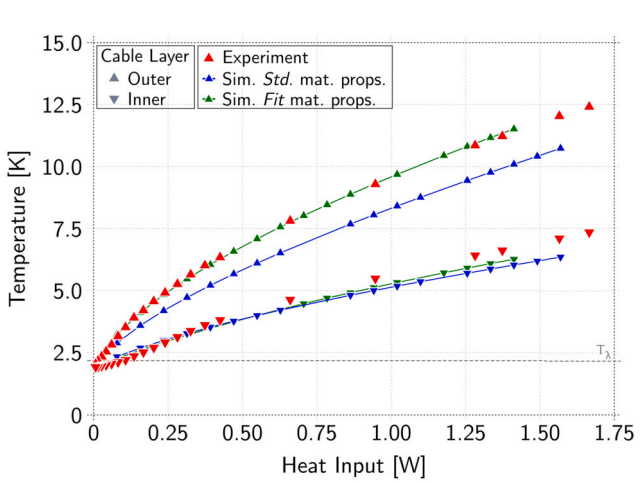

(a) Steady state temperatures for D11T-GE02 coil sample.

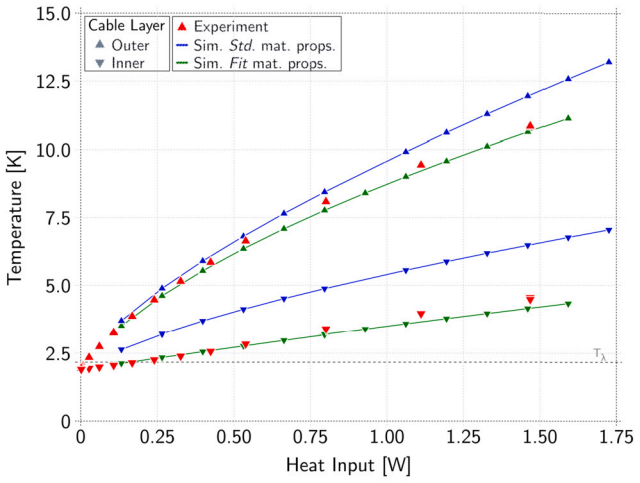

(b) Steady state temperatures for MQXF-P06 coil sample.

Fig. 7. Comparison between experimental vs. simulation results for steady state temperatures at bath temperature of 1.9 K.

An approach to integrate all the different solid material regions into a single-region mesh instead of defining separate regions or meshes for each one has been developed for the tool-kit. This has been done by allocating an integer index to each material in consideration. A separate *field* is supplied as an initial condition, which stores the material index for each cell of the mesh, according to the material it represents. The polynomial coefficients of the thermal properties, as supplied by the user, are read and stored in an instance of a material properties class at the beginning of the simulation. The diffusion coefficient or thermal conductivity has to be interpolated only using the harmonic mean for the entire mesh, ensuring conservation of heat flux at the cell faces where abrupt changes in conductivity, such as at the material interfaces, are seen. The solver uses the preconditioned bi-conjugate gradient stabilised method to solve the system of linear equations, which allows for asymmetric matrices as that for a composite system and also for a good parallel scaling.

The polynomial evaluation of the thermal properties of the solid materials has been implemented using Horner's method. With this method, for a polynomial of degree n, only n multiplications and n additions are needed instead of $(n^2+n)/2$ multiplications and n additions if the powers of each monomial are calculated individually.

The authors note that these implementations have lead to a gain in computation time by a factor of ~10 for the coil-sample simulation model of a single-region mesh, compared to a multi-region mesh. For the case study of the MQXF cold mass, a speedup ($t(1)/t(N)$ for N cores) of 2.55 for 12 threads in parallel processing with an Intel Xeon E5645 6-core processor is recorded.

A separate library dedicated to provide superfluid helium properties uses a C++ wrapper for HePak. This library also implements the local calculation of effective thermal conductivity, K_{eff} as described in section 3.3.

With respect to the interface boundary condition, two libraries implementing equation (10) have been created to be used either with a solid-conduction-only model or a conjugate heat transfer model.

Overall, the solvers and libraries have been developed following the object-oriented programming paradigm adopted by OpenFOAM. The functionality of the tool-kit may thus be easily upgraded, such as for normal liquid helium or vapor flow by following the same modular nature.

4. Use cases

The numerical modelling tool-kit thus developed has been applied to simulate three different cases, described in this section.

4.1. Coil samples - D11T & MQXF

Transient two-dimensional numerical simulations of the experimental studies on the two coil samples described in section 2 have been carried out for a bath temperature of 1.9 K. In this case study, the solid conduction model has been used and:

1. The cable stacks are approximated as a cable layer, *i.e.* inner and outer cable layers.
2. Each insulation layer, *i.e.* inner, inter-cable and outer layers, is modelled separately,
3. External insulation blocks are also modelled, to include heat losses to these layers compared to the coil samples.

The geometries are meshed with 0.12×10^6 tetrahedral prism cells, keeping conformal meshing at the boundaries of the different regions. Mesh convergence studies showed a requirement greater than 20 cells across the thickness of the thin insulation layers. A convergence criterion on residuals of time-step iteration is set on the temperature field to 1×10^{-6} K. The time step required for convergent transient simulations is 1 ms.

At the inner surface exposed to the bath, *i.e.* at that of the inner insulation layer, a Kapitza interface convection boundary condition is applied, with α and n values extracted from experimental data, and $T = 1.9$ K for bath temperature. A fixed Dirichlet boundary condition of $T = 1.9$ K is applied to all other external surfaces. A variation in the heat load from the polyimide heater is applied as a parameter.

In Fig. 7a and Fig. 7b, steady-state simulation results obtained using a *standard* thermal conductivity measurement data (shown in Fig. 5) for each coil sample are presented. In addition, iterative simulations have been carried out to *fit* the experimental data for T_{ss} and compare the thermal conductivity of these insulation layers. A typical sample case solution at steady-state is shown in Fig. 8 for the MQXF-P06 coil sample, with the variation in temperature along the mid-plane of the sample in the azimuthal direction, plotted in Fig. 9.

The usage of a single *standard* thermal conductivity data (G10 curve in Fig. 5) for the S2-glass epoxy resin insulation system for all the insulation layers of the magnet samples shows a significant deviation in simulation results (blue curves in Fig. 7a and Fig. 7b) from experimental data for both magnet samples. For the D11T-GE02 sample, an underestimation of steady state temperatures is reached, whereas they are overestimated for the MQXF-P06 sample.

The numerical simulations fitted to experimental data (green curves in these figures) can provide an estimation of the material properties for the different insulation layers, and are also plotted for comparison

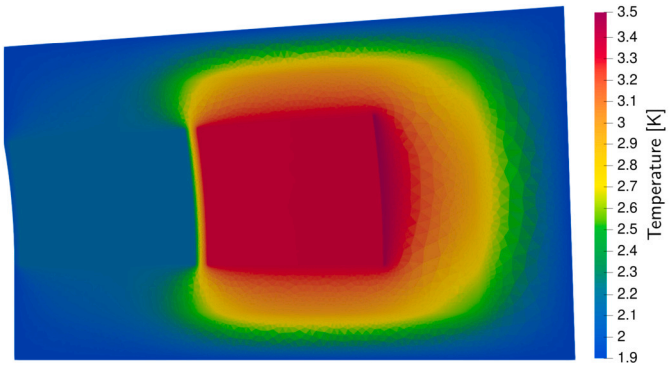

Fig. 8. Steady-state temperature map of the MQXF-P06 coil sample for a input heat load of 0.1 W from the foil heater on the outer surface of the sample.

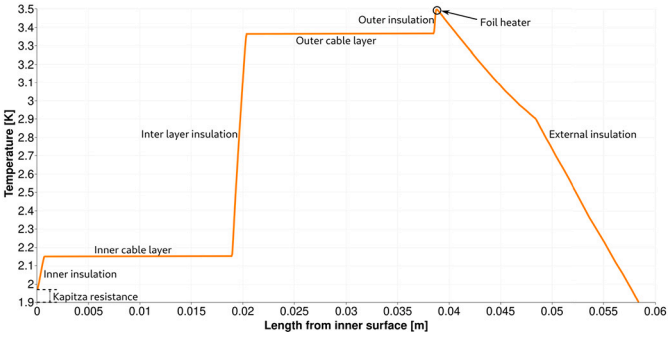

Fig. 9. Temperature profile along the mid-plane of coil sample MQXF-P06 for the simulation shown in Fig. 8.

in Fig. 5. A significant difference is seen between these four fits. This is especially evident for the inter layer insulation for both samples, which theoretically use the same insulation system (with different dimensions) and for which a similar thermal conductivity is expected. Between the two magnet samples, the D11T-GE02 sample shows lower heat transfer coefficients than the MQXF-P06 sample, by about a factor of 2. This is attributed to a difference in S2 glass fibre composition, interface resistances and possible difference in vacuum impregnation process or compression loads followed for the coils. The sensitivity of numerical simulations to parameters of the composite magnet, such as material properties (and dimensions) highlights the importance of having reasonably accurate material property measurements, and that these are relevant not only to the different magnet coil configurations in concern, but also to the interpretation of the experimental data and its usage for higher order magnet coil pack or complete cold mass simulations.

In Fig. 10a and Fig. 10b, time constants obtained using the *fit* thermal conductivity are shown. For the D11T-GE02 sample, an estimation of the helium content has been carried out, to be about ∼ 0.5 - 0.7% in the inner cable layer. This estimation would be expected to be reduced if the thermal conductivity of He II in the composite insulation layers is included. A comparison of transient behaviour obtained for MQXF-P06 sample shown in Fig. 10b bodes well for the raw heat capacity material properties used for the simulations.

4.2. Coil pack - D11T

A steady-state two-dimensional solid conduction heat transfer simulation of the D11T coil pack has been carried out as an intermediate step between those of the coil samples and a higher-level full cross-section of a magnet cold mass simulation. The geometry of the D11T coil pack is shown in Fig. 11. The peak power deposition map shown in Fig. 12 estimated by FLUKA simulations [48,49], assuming an instantaneous proton loss rate of 8.81×10^{11} protons/s, for a worst-case beam lifetime of 0.1 h, is used as input into the numerical model for this use-case.

In this case study, for the solid magnet region:

1. Each cable is represented separately as a single homogeneous region.
2. In the transverse direction, each cable insulation of 100 µm is modelled.
3. In the radial direction, the inner-, inter- and outer-layer insulations with thicknesses 350 µm, 500 µm, 100 µm, respectively, are modelled.
4. Other components, such as copper blocks, titanium pole wedges, and stainless steel loading plates are also represented.

At the inner radius, the Kapitza interface convection boundary condition for a solid-conduction simulation given by equation (10) is used. At the outer radius, a Dirichlet boundary condition of $T = 1.9$ K is applied. The converged mesh comprises $\sim 0.8 \times 10^6$ prismatic tetrahedral cells, maintaining conformity across the different material regions. It is worth reporting that the mesh convergence is mainly sensitive to the size and number of the cells in the thin-resistive regions.

The resulting temperature map obtained from the simulation is shown in Fig. 13 with the temperature profile along the radial direction at the mid-plane in the right half of the coil is shown in Fig. 14. A maximum temperature of 2.97 K is calculated, resulting in a temperature margin [50] of 4 K. The temperature profile indicates that the gradient at the inner surface is driven by an equal contribution from the Kapitza interface resistance and from the inner insulation layer of the coil pack.

4.3. Cold mass - MQXF

The Nb_3Sn inner triplet magnets (MQXF) have evolved since the initial thermal design requirements [51,52] provided during the mechanical design phase in 2015. Moreover, changes were made to the LHC optics and to the overall geometry of the magnets, affecting power deposition in the magnet cross-sections. Aiming to revise the temperature margins, two-dimensional simulations of a representative cross-section of the straight part of a MQXF cold mass have been carried out to reflect changes in both power deposition by beam collision debris and coil layout.

For each of the 12 MQXF magnets, the power density at the most exposed (peak) location has been mapped onto a detailed MQXF cold mass cross-section. The energy deposition in the inner triplet magnets in the insertion regions IR1 (ATLAS) and IR5 (CMS) used as input has been estimated by FLUKA for a baseline luminosity of 5×10^{34} cm^{-2} s^{-1}, for proton-proton collisions at a center-of-mass energy of 14 TeV, for HL-LHC optics v1.5 released in 2019 [53]. The resulting temperature profile, that takes into account the heating due to the collision-induced power deposition, allows for a reassessment of the local temperature margins of each magnet at its most exposed location. A detailed description of the numerical assessment carried out for the MQXF magnets, as well as the considered operating conditions, can be found in [54].

In Fig. 15, the mesh for the MQXF geometry including the stagnant He II bath, with special refinement on thin layers such as the inter-cable insulation and the helium passages throughout the cold mass, is shown. The refinement level of this mesh, consisting of 3.5 M prismatic cells and following the conformal requirements of the numerical tool-kit, is obtained after a convergence study.

As an example of the results obtained for the full study, Fig. 16 and Fig. 17 show the power deposition map and resulting simulated temperature profile, respectively, for the most exposed cross-section of MQXF magnet Q3A, in IR5 (CMS). The highest power density is concentrated in the beam pipe, where it reaches a peak value of 5 mW cm^{-3}, and in the inner layer of the magnet coil, where the maximum is 2.7 mW cm^{-3}. The resulting temperature profile reflects this, as the highest temperature (2.7 K) is found in the magnet's cold bore. On the coil pack, however,

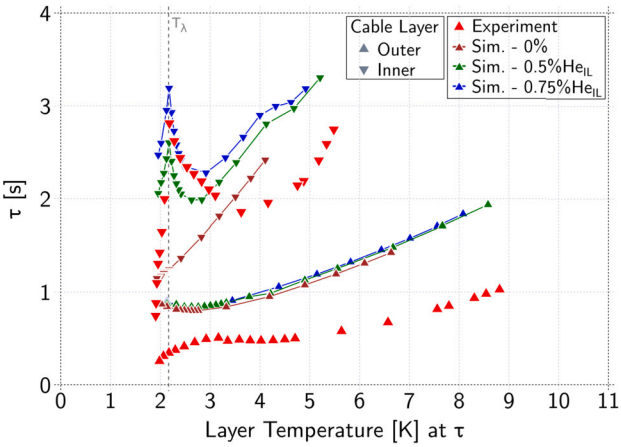

(a) Time constants for D11T-GE02 coil sample.

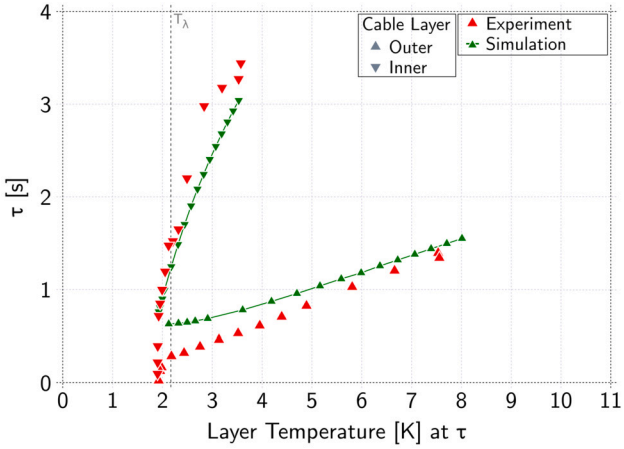

(b) Time constants for MQXF-P06 coil sample.

Fig. 10. Comparison between experimental and simulation results for time constants, at bath temperature of 1.9 K.

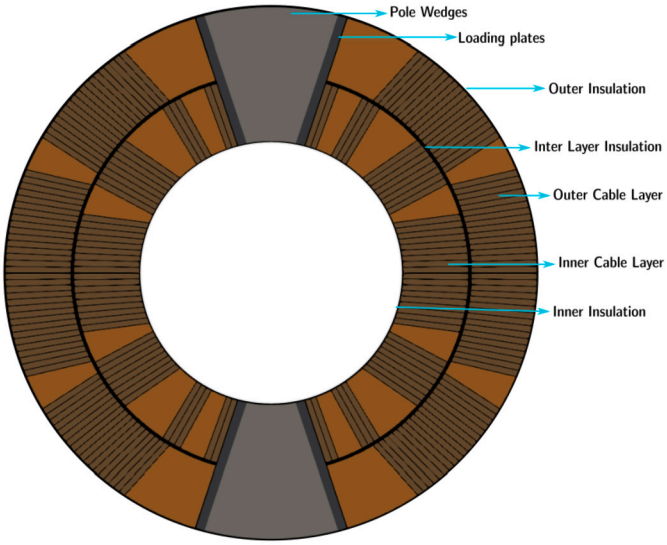

Fig. 11. Geometry of the D11T coil pack.

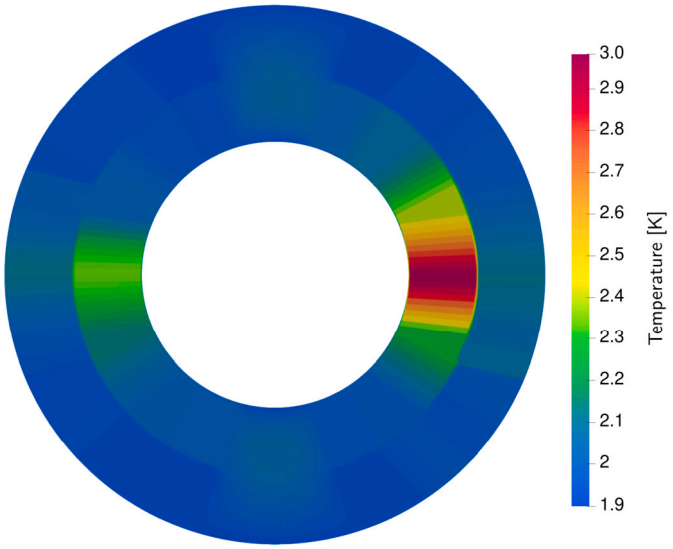

Fig. 13. Simulated temperature field of the D11T coil pack at peak location.

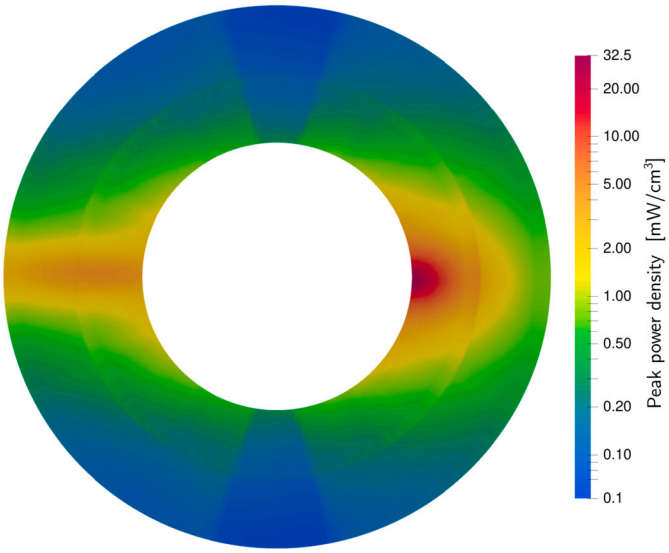

Fig. 12. 2D energy deposition map at peak location at end of MBHB D11T magnet.

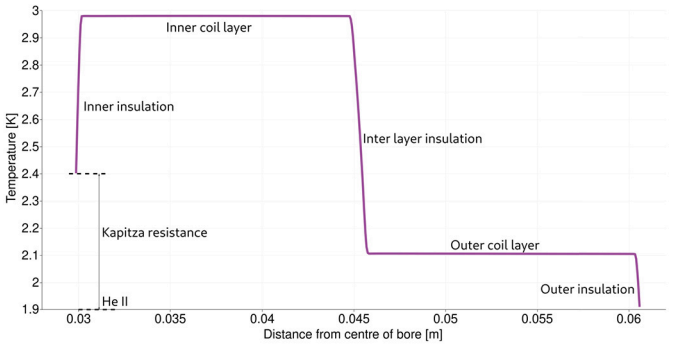

Fig. 14. Temperature profile along the mid-plane of the right half of the coil pack, detailing the contribution of the various components.

the maximum temperature is calculated as 2.2 K, resulting in a temperature margin [2] of 4.78 K.

The temperature profile along the radial direction indicates that the temperature gradient in this direction is dominated by the inner insulation on the coil pack, followed by the interlayer insulation (O(200 mK)) and finally, to a lesser extent, by the Kapitza interface resistance (O(30 mK)).

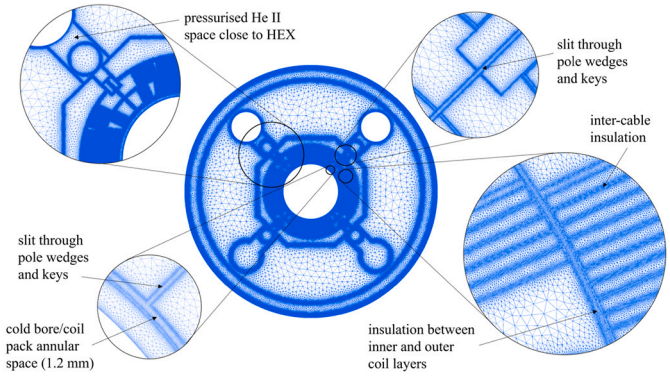

Fig. 15. Conformal mesh for the MQXF cold mass, including the cold bore, showing details concerning the He II passageways and the thin insulation layers in the coil and between each cable.

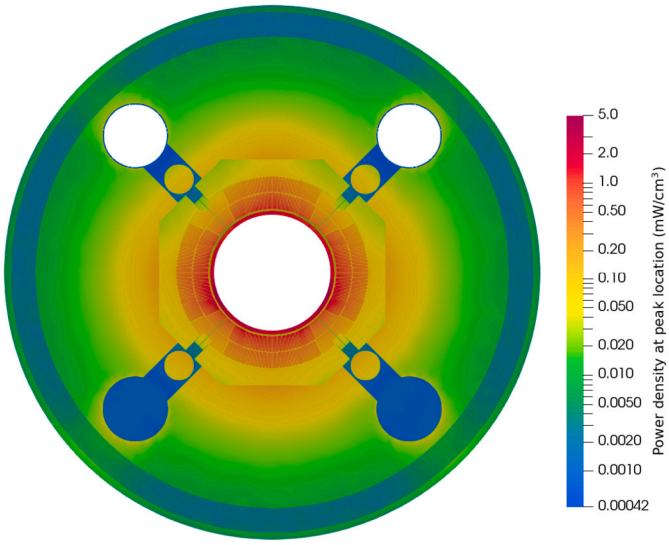

Fig. 16. Power density at peak location for Q3A in IR5 considering a luminosity of 5×10^{34} cm^{-2} s^{-1} and baseline cold source at 1.9 K.

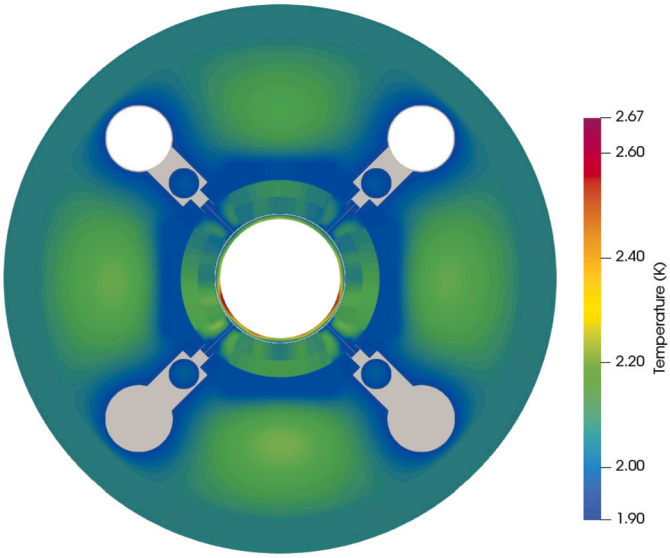

Fig. 17. Temperature profile at peak location for Q3A in IR5 considering a luminosity of 5×10^{34} cm^{-2} s^{-1} and baseline cold source at 1.9 K.

5. Conclusions

Building on the foundation of experimental measurements on NbTi superconducting cables, a successful test program for the Nb_3Sn magnet coil samples for the HL-LHC has been carried out. The next phase of the experiments involves evaluating the coil samples under thermal cycling, to assess the evolution of He content measured within the samples. In parallel, a robust, easily adaptable numerical toolkit has been developed to evaluate the heat transfer mechanisms in complex magnet geometries cooled by superfluid helium. An efficient workflow with low computational cost has enabled applying the toolkit to several use cases. However, the numerical model is capable of handling only heat transfer from static superfluid helium. The next phase involves upgrading its capabilities to handle problems involving normal helium and two-phase flow.

An important observation from the experimental studies is that the thermal properties of the thin insulation layers may vary with composition or fabrication technique. These resistive insulation layers drive the heat transfer behaviour of the magnets, and their impact is heavily seen on numerical solutions as well, *i.e.* a small variation in either dimension or thermal conductivity can result in relatively large deviation in the solution. Numerical simulations necessary for the MQXF cold mass, using the material property data obtained from the experimental test campaign and extracted using a parametric numerical analysis, have been carried out for several power density load cases [54].

CRediT authorship contribution statement

Kirtana Puthran: Conceptualization, Data curation, Formal analysis, Investigation, Methodology, Software, Validation, Visualization, Writing – original draft, Writing – review & editing. **Patricia Borges de Sousa:** Conceptualization, Data curation, Formal analysis, Investigation, Methodology, Visualization, Writing – original draft, Writing – review & editing. **Lise Murberg:** Conceptualization, Data curation, Formal analysis, Investigation, Methodology, Validation, Visualization, Writing – original draft. **Torsten Koettig:** Conceptualization, Funding acquisition, Investigation, Methodology, Project administration, Resources, Supervision, Writing – review & editing. **Rob van Weelderen:** Conceptualization, Formal analysis, Funding acquisition, Investigation, Methodology, Project administration, Resources, Software, Supervision, Validation, Writing – review & editing.

Declaration of competing interest

The authors declare that they have no known competing financial interests or personal relationships that could have appeared to influence the work reported in this paper.

Data availability

Data will be made available on request.

Acknowledgement

This work was supported by the HL-LHC Project.

The authors sincerely thank Agostino Vacca, Laetitia Dufay-Chanat, Johan Bremer from TE-CRG-CI, Stephane-Triquet, Steve Becle, Susana Izquierdo Bermudez of TE-MSC-LMF and Andreas Waets, Marta Sabate Gilarte, Anton Lechner of SY-STI at CERN, and Jesse Schamlzle, Miao M Hu, Georgio Ambrosio of Fermilab for their essential contributions to this project.

References

[1] Meuris C. Heat transport in insulation of cables cooled by superfluid helium. Cryogenics 1991;31(7):624–8.

[2] Aberle O, et al. High-Luminosity Large Hadron Collider (HL-LHC): technical design report. CERN yellow reports: monographs. Geneva: CERN; 2020. Available from: https://cds.cern.ch/record/2749422.

[3] Granieri Pier Paolo, van Weelderen Rob. Deduction of steady-state cable quench limits for various electrical insulation schemes with application to lhc and hl-lhc magnets. IEEE Trans Appl Supercond 2014;24(3):1–6. https://doi.org/10.1109/TASC.2014.2299797.

[4] Lebrun P, Tavian L. Cooling with superfluid helium. In: Bailey R, editor. CAS-CERN accelerator school: superconductivity for accelerators; 2014. p. 453–76. Available from: https://cds.cern.ch/record/1974065.

[5] Winkler Tiemo. Helium II Heat Transfer in LHC magnets: polyimide cable insulation. PhD thesis. Netherlands: University of Twente; June 2017.

[6] Martins Galinhas Bruno Emanuel. Study of helium II heat transport phenomena in superconducting Rutherford type cables. Available from: http://cds.cern.ch/record/2640643, 2015. Presented on Mar. 2015.

[7] Grosso Xavier Mário D, Schundelmeier Jens, Winkler Tiemo, Koettig Torsten, van Weelderen Rob, Bremer Johan. Transient heat transfer in superfluid helium cooled nb _3 sn superconducting coil samples. IEEE Trans Appl Supercond 2019;29(5):1–5.

[8] Murberg Lise. Heat transfer to he ii in hl-lhc magnet samples - d11tge02. Available from: https://edms.cern.ch/document/2907047/1, 2020. EDMS document no. 2907047.

[9] Savary Frederic, Bajko Marta, Bordini Bernardo, Bottura Luca, Fiscarelli Lucio, Fleiter Jerome, et al. Progress on the development of the nb3sn 11t dipole for the high luminosity upgrade of lhc. IEEE Trans Appl Supercond 2017;27(4):1–5.

[10] Todesco E, Bajas H, Bajko M, Ballarino A, Izquierdo Bermudez S, Bordini B, et al. The high luminosity lhc interaction region magnets towards series production. Supercond Sci Technol mar 2021;34(5):053001. https://doi.org/10.1088/1361-6668/abdba4.

[11] Izquierdo Bermudez Susana, Ambrosio Giorgio, Apollinari Giorgio, Bajko Marta, Bordini Bernardo, Bourcey Nicolas, et al. Progress in the development of the nb3sn mqxfb quadrupole for the hilumi upgrade of the lhc. IEEE Trans Appl Supercond 2021;31(5):1–7. https://doi.org/10.1109/TASC.2021.3061352.

[12] Axensalva Jerome, Lackner Friedrich, Gauthier Remy. Vacuum pressure impregnation setup at CERN for Nb_3Sn coils. IEEE Trans Appl Supercond June 2020;30(4):1–4.

[13] Field Michael B, Zhang Youzhu, Miao Hanping, Gerace Michael. Optimizing nb_3sn conductors for high field applications. IEEE Trans Appl Supercond 2013;24(3):1–5.

[14] Cooley LD, Ghosh AK, Dietderich DR, Pong I. Conductor specification and validation for High-Luminosity LHC quadrupole magnets. IEEE Trans Appl Supercond June 2017;27(4):1–5.

[15] Fleiter Jerome, Ballarino Amalia, Bonasia Angelo, Bordini Bernardo, Richter David. Optimization of Nb_3Sn rutherford cables geometry for the High-Luminosity LHC. IEEE Trans Appl Supercond June 2017;27(4):1–5.

[16] Devred Arnaud. Insulation systems for nb_3sn accelerator magnet coils manufactured by the wind & react technique. IEEE Trans Appl Supercond 2002;12(1):1232–7.

[17] Salome Platform - the open-source platform for numerical simulation. Available from: https://www.salome-platform.org/.

[18] The OpenFOAM Foundation. Available from: https://openfoam.org/.

[19] Van Sciver SW. Helium cryogenics. International cryogenics monograph series. New York: Springer. ISBN 9781441999795, 2012.

[20] Arp V. Heat transport through helium II. Cryogenics 1970;10(2):96–105.

[21] Cody GD, Cohen RW. Thermal conductivity of nb 3 sn. Rev Mod Phys 1964;36(1):121.

[22] Rondeaux F, Bredy Ph, Rey JM. Thermal conductivity measurements of epoxy systems at low temperature. AIP Conf Proc 2002;614:197–203. American Institute of Physics.

[23] Ekin Jack. Experimental techniques for low-temperature measurements: cryostat design, material properties and superconductor critical-current testing. Oxford University Press; 2006.

[24] Bauer P, Rajainmaki H, Salpietro E. Efda material data compilation for superconductor simulation 2007;7:67.

[25] den Ouden A, van Oort JM, ten Kate HHJ, van de Klundert LJM, Burnod L. Thermal conduction in fully impregnated nb 3 sn windings for lhc type of dipole magnets. In: Advances in cryogenic engineering materials, vol. 38, Part B. 1992.

[26] Baudouy B, Polinski J. Thermal conductivity and kapitza resistance of epoxy resin fiberglass tape at superfluid helium temperature. Cryogenics 2009;49(3–4):138–43.

[27] Pietrowicz S, Four A, Jones S, Canfer S, Baudouy B. Thermal conductivity and kapitza resistance of cyanate ester epoxy mix and tri-functional epoxy electrical insulations at superfluid helium temperature. Cryogenics 2012;52(2–3):100–4.

[28] Vieland LJ, Wicklund AW. Specific heat of niobium-tin. Phys Rev 1968;166(2):424.

[29] Wang Yuxing, Senatore Carmine, Abächerli V, Uglietti Davide, Flükiger R. Specific heat of nb3sn wires. Supercond Sci Technol 2006;19(4):263.

[30] Woodcraft Adam L, Gray Adam. A low temperature thermal conductivity database. In: Aip conference proceedings, vol. 1185. American Institute of Physics; 2009. p. 681–4.

[31] Polinski J, Bogdan P, Chorowski M, Niechcial J, Noga A, Pyrka P. Thermal properties of larp type nb3sn superconducting magnet coil electrical insulation in pressurized superfluid helium. J Supercond Nov Magn 2015;28(2):633–7.

[32] Rossi Lucio, Sorbi Massimo. Matpro: a computer library of material property at cryogenic temperature. Technical report. 2005.

[33] Marquardt ED, Le JP, Radebaugh Ray. Cryogenic material properties database. Cryocoolers 2002;11:681–7.

[34] Davies Andrew. Material properties data for heat transfer modeling in nb3sn magnets. Ill Accel Inst 2011;17:1–53.

[35] de Sousa Patricia B. Thermal conductivity measurement report - 11 t dipoles sample # 8. Available from: https://edms.cern.ch/document/2042486/1, 2018. EDMS document no. 2042486.

[36] Koettig T, Maciocha W, Bermudez S, Rysti J, Tavares S, Cacherat F, et al. Thermal conductivity measurements of impregnated nb3sn coil samples in the temperature range of 3.5 k to 100 k. IOP conference series: materials science and engineering, vol. 171. IOP Publishing; 2017. p. 012103.

[37] HEPAK version 3.4, Cryodata Inc. P.O. Box 173, Louisvile, CO 80027.

[38] 46 - the theory of superfluidity of helium II, Ter Haar D, editor. Collected papers of L.D. Landau. Pergamon. ISBN 978-0-08-010586-4, 1965. p. 301–30.

[39] Gorter CJ, Mellink JH. On the irreversible processes in liquid helium II. Physica 1949;15(3):285–304. https://doi.org/10.1016/0031-8914(49)90105-6.

[40] Sato A, Maeda M, Kamioka Y. Steady state heat transport in a channel containing he ii at high pressures up to 1.5 mpa. AIP Conf Proc 2004;710(1):999–1006. https://doi.org/10.1063/1.1774782.

[41] Sato A, Maeda M, Kamioka Y. Chapter 201 - normalized representation for steady state heat transport in a channel containing he ii covering pressure range up to 1.5 mpa. In: Zhang Liang, Lin Liangzhen, Chen Guobang, editors. Proceedings of the twentieth international cryogenic engineering conference (ICEC20). Oxford: Elsevier Science. ISBN 978-0-08-044559-5, 2005. p. 849–52.

[42] Lebrun Philippe, Tavian Laurent. The technology of superfluid helium. In: Proc. CERN accelerator school superconductivity and cryogenics for accelerators and detectors, CERN-2004-008; 2004. p. 375–95.

[43] Nakai Hirotaka, Kimura Nobuhiro, Murakami Masahide, Haruyama Tomiyoshi, Yamamoto Akira. Superfluid helium flow through porous media. Cryogenics 1996;36(9):667–73.

[44] Baudouy B, Juster F-P, Allain H, Prouzet E, Larbot A, Maekawa R. Heat transfer through porous media in static superfluid helium. AIP Conf Proc 2006;823:409–16. American Institute of Physics.

[45] Allain Hervé, Baudouy Bertrand, Quintard Michel, Prat Marc. Experimental investigation of heat transfer through porous media in superfluid helium. Cryogenics 2015;66:53–62.

[46] Soulaine Cyprien, Quintard Michel, Allain Hervé, Baudouy Bertrand, Van Weelderen Rob. A piso-like algorithm to simulate superfluid helium flow with the two-fluid model. Comput Phys Commun 2015;187:20–8.

[47] Allain H, Quintard Michel, Prat Marc, Baudouy B. Upscaling of superfluid helium flow in porous media. Int J Heat Mass Transf 2010;53(21–22):4852–64.

[48] Lechner A, Auchmann B, Baer T, Bahamonde Castro C, Bruce R, Cerutti F, et al. Validation of energy deposition simulations for proton and heavy ion losses in the cern large hadron collider. Phys Rev Accel Beams 2019;22(7):071003.

[49] Waets Andreas, Sabaté-Gilarte Marta, Belli Eleonora, Bruce Roderik, Redaelli Stefano, Mereghetti Alessio, et al. Power deposition in superconducting dispersion suppressor magnets downstream of the betatron cleaning insertion for hl-lhc; 2021.

[50] Izquierdo Bermudez S, Auchmann Bernhard, Bajas Hugues, Bajko Marta, Bordini Bernardo, Bottura Luca, et al. Quench protection studies of the 11-t nb 3 sn dipole for the lhc upgrade. IEEE Trans Appl Supercond 2016;26(4):1–5.

[51] Bozza Gennaro, Malecha Ziemowit M, van Weelderen Rob. Development and application of a generic cfd toolkit covering the heat flows in combined solid–liquid systems with emphasis on the thermal design of hilumi superconducting magnets. Cryogenics 2016;80:253–64. https://doi.org/10.1016/j.cryogenics.2016.04.007. Chats on Applied Superconductivity 2015 University of Bologna, Italy, 14-16 September 2015.

[52] Bozza Gennaro. Thermal design of HiLumi-LHC insertion magnets. Available from: https://edms.cern.ch/document/1531858/1, 2015. EDMS document no. 1531858.

[53] Sabaté-Gilarte Marta, Cerutti Francesco. Energy deposition study of the CERN HL-LHC optics v1.5 in the ATLAS and CMS insertions; 2021. p. 76–9. Available from: http://cds.cern.ch/record/2783808.

[54] Borges de Sousa Patricia, Puthran Kirtana, Sabaté-Gilarte Marta, Cerutti Francesco, Izquierdo Bermudez Susana, Todesco Ezio, et al. Numerical assessment of the inhomogeneous temperature field and the quality of heat extraction of nb3sn impregnated magnets for the high luminosity upgrade of the lhc. IEEE Trans Appl Supercond 2023;33(5):1–5. https://doi.org/10.1109/TASC.2023.3240126.